# Quantification of Optical and Physical Properties of Combustion-Generated Carbonaceous Aerosols (< PM$_{2.5}$) Using Analytical and Microscopic Techniques

*Inoka Eranda Perera\* and Charles D. Litton, Pittsburgh Research Laboratory, Fires and Explosions Branch, Office of Mine Safety and Health Research, National Institute for Occupational Safety and Health, Centers for Disease Control & Prevention, U. S. Department of Health & Human Services, 626 Cochrans Mill Road, PO Box 18070, Pittsburgh, PA 15236, USA e-mail: clitton@cdc.gov*

**Abstract.** A series of experiments were conducted to quantify and characterize the optical and physical properties of combustion-generated aerosols during both flaming and smoldering combustion of three materials common to underground mines—Pittsburgh Seam coal, Styrene Butadiene Rubber (a common mine conveyor belt material), and Douglas-fir wood—using a combination of analytical and gravimetric measurements. Laser photometers were utilized in the experiments for continuous measurement of aerosol mass concentrations and for comparison to measurements made using gravimetric filter samples. The aerosols of interest lie in the size range of tens to a few hundred nanometers, out of range of the standard photometer calibration. To correct for these uncertainties, the photometer mass concentrations were compared to gravimetric samples to determine if consistent correlations existed. The response of a calibrated and modified combination ionization/photoelectric smoke detector was also used. In addition, the responses of this sensor and a similar, prototype ionization/photoelectric sensor, along with discrete angular scattering, total scattering, and total extinction measurements, were used to define in real time the size, morphology, and radiative transfer properties of these differing aerosols that are generally in the form of fractal aggregates. SEM/TEM images were also obtained in order to compare qualitatively the real-time, continuous experimental measurements with the visual microscopic measurements. These data clearly show that significant differences exist between aerosols from flaming and from smoldering combustion and that these differences produce very different scattering and absorption signatures. The data also indicate that ionization/photoelectric sensors can be utilized to measure continuously and in real time aerosol properties over a broad spectrum of applications related to adverse environmental and health effects.

---

\* Correspondence should be addressed to: Inoka Eranda Perera, E-mail: eperera@cdc.gov

**List of Symbols**

| | |
|---|---|
| $d_g$ | Number mean Diameter |
| $D_f$ | Fractal dimension |
| $d_p$ | Diameter of primary particles (nm) |
| $d_{10}$ | Count mean diameter (cm) |
| $D_i$ | Ion diffusion coefficient ($cm^3$/s) |
| $I_0$ | Incident intensity of the light |
| $I$ | Reduced intensity of light |
| $k_f$ | Fractal pre-factor |
| $l$ | Path length (m) |
| $M$ | Aerosol mass concentration ($mg/m^3$) |
| $M_a$ | Mass of a fractal aggregate |
| $n_p$ | Number of primary particles per aggregate |
| $N$ | Number of aggregate per $cm^3$ |
| $R_g$ | Radius of gyration |
| $x_p$ | Size parameter |
| $\sigma_{ext}$ | Mass specific extinction ($m^2$/g) |
| $\sigma_{sca}$ | Mass specific scattering ($m^2$/g) |
| $\sigma_{abs}$ | Mass specific absorption ($m^2$/g) |
| $\lambda$ | Wavelength (nm) |
| $\rho_p$ | Particle density ($g/m^3$) |

# 1. Introduction

Carbonaceous aerosols generated from a variety of combustion sources generally appear as fractal aggregates of various shapes and sizes, depending upon the mode of combustion, the combustible material, and so on. Aerosols generated from internal combustion engines, such as diesels, or from open and well-ventilated flaming fires, tend to produce fractal aggregates of mostly carbon (i.e., black carbon aerosols/soot) with relatively small primary particles and elongated, chain-like morphologies, while those produced from fuel-rich fires and smoldering surface fires of solid combustibles tend to have lower levels of carbon, larger primary particles, and clumped or more densely packed morphologies [19]. Both types of aerosols generally have maximum average dimensions in the range of 200 to 500 nm but their radiative transfer properties (scattering, absorption, extinction) can vary dramatically. Fractal aggregates are generally characterized by a set of parameters that include the fractal, or Hausdorff dimension, $D_f$, the radius of gyration, $R_g$, the diameter, $d_p$, of each primary particle forming the aggregate, and the average number of these primary particles per aggregate, $n_p$. The fractal dimension is generally a measure of the shape of the aggregate, where values in the range of 1.6 to 1.9 correspond to aggregates that have an elongated, chain-like structure with very little overlap of individually connected particles. Higher fractal dimensions, generally in the range of 2.1 to 2.3, correspond to aggregates that are more compact, with individual particles significantly overlapped or necked together.

Another critical parameter in the quantification of optical and physical properties of aerosols is the measurement of the aerosol mass concentration. There are many techniques available to make this measurement, and some of the more commonly used instruments for real-time or near real-time mass concentration measurements include the Tapered Element Oscillating Microbalance (TEOM), TSI Scanning Mobility Particle Sizer (SMPS), Aerodynamic Particle Sizer (APS), TSI Condensation Particle Counter (CPC), TSI DustTrak, Dekati Electrical Low Pressure Impactor (ELPI), beta attenuation monitor (BAM), continuous aerosol mass monitor (CAMM), MiniVol, and so on [4, 7–9, 16, 22]. While these instruments are available at varying levels of cost and complexity, it has been reported that some instruments suffer from problems due either to the type of measurement or to the electronics used to process the signals. In some cases sample artifacts make data interpretation more difficult [3]. There are only a few studies available in the literature that compare different methods and instruments for continuous measurement of aerosol mass concentrations. Of the comparison studies available, Moosmuller et al. [16], Kelly and Mcmurry [7] and Anderson noted that the TEOM agreed well with the gravimetric measurements using a time constant correction factor [9]. Chung et al. [4] found that BAM and CAMM correlate well with filter-based measurements for monitoring $PM_{2.5}$ airborne particulate matter. Yanosky et al. [22] noted that in comparison to the FRM (Federal Reference method) samples, APS measurements were less precise and less accurate [22].

In the present study, DustTrak mass measurements were compared to both gravimetric mass measurements and the mass measurements obtained from a modified and previously calibrated combination ionization/photoelectric UCB smoke sensor. The UCB device is used here to validate its accuracy as a simple device and technique to define properties of smoke generated from different combustible materials. The DustTrak instruments were chosen on the basis of lower cost, portability, higher signal to noise ratio, less interference from non-particulate sources or gases, and ease of use/calibration. SEM/TEM images were also obtained for smoke generated from flaming and smoldering materials in order to analyze the size and morphology of the aggregates and to compare these analyses with those obtained using the other experimental data.

Because the DustTrak generally overestimates the mass concentration, it is important, if possible, to quantify correction factors or expressions that can be used to reduce the data and obtain accurate aerosol mass concentrations. The DustTrak operates on the principle of light scattering using a laser diode that emits at a wavelength of 780 nm. The chamber of the DustTrak is designed with a lens that is positioned at 90° to both the aerosol stream and laser beam and focuses the scattered light into a photodiode. The signal from the photodiode is converted into voltage which is directly proportional to the aerosol mass concentration. Since the instrument is calibrated specifically with Arizona road dust (typically $PM_{10}$ or $PM_{2.5}$), the factory calibration may not apply to all types of aerosol generated from various combustion sources. Many reported studies use a correction factor of 3 or less when measuring aerosol mass concentration using a DustTrak, especially when analyzing diesel particular matter or $PM_{2.5}$ [8, 10, 16, 18, 22]. In the current study, the TSI DustTrak (Models 8530 and 8520)

measurements were compared with the gravimetric mass measurements for aerosols generated from both flaming and smoldering fires of different combustion sources, including pulverized Pittsburgh seam coal, Douglas-fir wood chips, and styrene butadiene rubber (SBR) conveyor belt in order to determine an accurate DustTrak calibration factor that could be used for combustion-generated aerosols with diameters in the range of 0.010–1.0 μm in diameter.

Even though smoke detectors are primarily used to monitor and detect smoke for purposes of fire protection, the feasibility of using a modified smoke detector as a low-cost particle monitoring device is also discussed in this study. It has been observed that ionization-type smoke detectors respond better to the smaller diameter particles produced from flaming combustion, while the photoelectric-type smoke detectors respond better to the larger diameter particles produced from smoldering combustion [2, 14, 15, 17, 21]. Additional research conducted by NIOSH reveals that the ionization-type detector also shows a high response to smaller particles produced from the exhausts of diesel engines, while the photoelectric type detector shows a much lower response [11]. For the larger particles produced from smoldering combustion, the reverse is true. In a previous study using the UCB sensor, it was shown that both the optical and ionization responses per unit aerosol mass and aerosol surface concentrations correlated with the ratio of ionization to photoelectric signals, and were in opposite directions [13]. In order to further investigate the UCB sensor as a low-cost particle monitor, the outputs of the photoelectric and ionization chambers were recorded and the data reduced using a simple theory (discussed below) to calculate properties of the smoke aggregates as well as the aerosol mass concentrations for comparison to the DustTrak measurements. In addition to the UCB sensor, the responses of a similar prototype optical/ionization detector (OPTION sensor) that measures angular scattering at two forward angles, along with the response of an ionization chamber, were also obtained and used to calculate the properties of the aggregates for comparison with the UCB sensor data and the DustTrak and gravimetric mass measurements [13]. Overall, the size, morphology and indirectly, the chemistry, of aerosols produced from a variety of mine combustibles can vary significantly, making such aerosols more (or less) difficult to detect, thereby impacting the performance of smoke sensors used for fire detection and making the hazards (visibility and toxicity) produced from fires more (or less) severe. Quantifying and subsequently correlating aerosol properties with fire detection and fire hazard is one important step towards improving underground fire safety.

## 2. Theory and Background

The chemistry, morphology, and size of fractal aggregates produced from combustion aerosols vary depending on the source and the nature of the fire from which they are generated, and these properties, in turn, produce unique scattering and extinction properties. Farias et al. [6] and Sorensen [20] have used light scattering signatures (intensity versus angle) to derive average size (radius of gyration, $R_g$)

and fractal dimension, $D_f$, through the use of $q$, the modulus of the scattering vector, defined in Eq. (1).

$$q = \frac{4\pi}{\lambda} \sin(\theta/2) \tag{1}$$

where $\theta$ is the scattering angle measured from the forward direction and $\lambda$ is the wavelength, either 635 or 532 nm for the work reported here. For small angles, and with $qR_g < 1$, scattering is in the so-called Guinier regime where the intensity is independent of the index of refraction and given approximately by the Guinier equation, as in Eq. (2).

$$I(q) \approx 1 - (1/3)(qR_g)^2 \tag{2}$$

Similarly, for large values of $q$ and $qR_g \gg 1$, the angular intensity varies according to Eq. (3).

$$I(q) \approx q^{-D_f} \tag{3}$$

Thus, for small $q$, a plot of $I(q)$ versus $q^2$ yields the radius of gyration, $R_g$, while at large $q$, $\ln(I(q))$ versus $\ln(q)$ yields the fractal dimension, $D_f$. For the aggregate particles, the applicable fractal power law is given by Eq. (4).

$$n_p = k_f (R_g/d_p)^{D_f} \tag{4}$$

Since $R_g$ and $D_f$ can be obtained from the angular scattering data, the primary particle diameter is the remaining parameter to be determined. Generally, SEM or TEM measurements provide sufficient information to determine $d_p$, but these techniques are unable to provide continuous, real-time information. To determine approximate values of $d_p$, the response of the ionization chamber from either the UCB or OPTION sensor is used in the following manner. For voltage changes less than about 1 to 1.2 V, the change in voltage from the ionization chamber can be approximated using a Taylor series expansion that leads to the linear Eq. (5), where $d_g$ is the number mean diameter, $d_{10}$ is the count mean diameter, and $d_{30}$ is the diameter of average mass [12, 13].

$$\Delta CEV = (0.075)2\pi D_i d_{10} N \tag{5}$$

The mass concentration, $M$, in mg/m$^3$, can be expressed by Eq. (6).

$$M = 1 \times 10^9 (\pi/6)(d_{30})^3 N \tag{6}$$

The ratio $CEV/M$, for an aggregate size distribution that is assumed to be lognormal with a geometric standard deviation of $\sigma_g = 1.70$, is given by Eq. (7) [12, 13].

$$CEV/M = 2.918 \times 10^{-10} D_i/d_g^2 \tag{7}$$

In a previous study using the UCB sensors, $D_i$ was found to have a value of 0.1522 cm$^2$/s, although a generally accepted minimum value is much lower at 0.042 cm$^2$/s. For the studies reported here, a value of $D_i$ equal to 0.0646 cm$^2$/s is used and it should be noted that the classic Langevin theory for determination of $D_i$ yields a similar value of 0.06631 cm$^2$/s at standard temperature and pressure. Using $D_i = 0.0646$, Eq. (7) can be rearranged to yield $d_g$ [12, 13].

$$d_g = 4.342 \times 10^{-6}/(CEV/M)^{1/2} \tag{8}$$

For the assumed lognormal distribution with $\sigma_g = 1.70$, $d_{10}$ is 1.15 times $d_g$, and using the value of $D_i = 0.0646$ cm$^2$/s, Eq. (5) can then be rearranged to yield the following expression for $N$.

$$N = 28.54(CEV/d_g) \tag{9}$$

Since the aerosol mass concentration is the average mass of an aggregate, $M_a$, times the number concentration, $N$, $M_a$ is given by the simple Eq. (10).

$$M_a = (1 \times 10^{-9})(M/N) \tag{10}$$

Similarly, the mass of an aggregate is the mass of an individual primary particle (particle density, $\rho_p$, × particle volume, $\pi d_p^3/6$) times the average number of primary particles per aggregate. Using Eq. (4), the average mass of an aggregate can then be expressed as in Eq. (11).

$$M_a = k_f (R_g/d_p)^{D_f} \rho_p \pi d_p^3 /6 \tag{11}$$

And solving this expression for $d_p$ yields Eq. (12).

$$d_p = [(6/\pi)(M_a/(k_f \rho_p R_g^{D_f}))]^{1/(3-D_f)} \tag{12}$$

Once $d_p$ is determined, the average number of primary particles per aggregate can then be determined. It should be noted that Eq. (11) implicitly assumes that the primary particles forming the aggregate just barely touch and that no overlap occurs. In general, this is approximately true for fractal aggregates (FAs) with $D_f$ in the range of 1.7 to 1.9, but for higher fractal dimensions, significant overlap does occur, and this should be accounted for in the above expressions.

In order to calculate the mass using the UCB sensor, the relationship between the ionization chamber response and the optical scattering chamber response was used. The ionization chamber sensitivity, $CEV/M$, and the optical scattering sensitivity, $V_{45}/M$, correlate with the dimensionless ratio, $CEV/V_{45}$, over a broad range of aerosol diameters as shown in Fig. 1 [12]. Detailed theory and calculations using this instrument can be found elsewhere [11, 12]. The calibration plot in Fig. 1 and the resultant empirical correlations were used to calculate the UCB mass measurements presented in this study.

## 3. Experimental Details

Experiments were conducted using a standard Underwriters Laboratory Inc. (UL 268) smoke chamber connected to a combustion chamber containing a circular disk heater that was used to heat the solid combustibles [5]. The combustible materials used in both flaming and smoldering experiments were wood chips from dried Douglas-fir, Pittsburgh seam coal ($-9.4$ to $+6.7$ mm mesh) and styrene butadiene rubber (SBR) from a typical non-fire resistant conveyor belt.

Once in the smoke chamber, the aerosol was mixed uniformly using two small circulating fans. Inside the smoke chamber, optical density of the aerosol was measured over a 1.48-m optical path length using an incandescent lamp and a standard photocell with spectral response matching the spectral response of the human eye. In some of the earlier experiments, light extinction over a 0.65-m path at a wavelength of 532 nm was also measured within the smoke chamber using a small laser and silicon photodiode. Also, the modified UCB smoke sensor was placed inside the smoke chamber and its response was obtained through a microprocessor. During the experiments, the aerosols were continuously extracted from the smoke chamber using metal tubes inserted into the top of the smoke box and flowed to various measuring devices.

In addition to the measurements of visible light obscuration and light extinction at 532 nm, data acquired during the experiments also included discrete angular scattering at wavelengths of 635 nm and 532 nm and at four forward and two
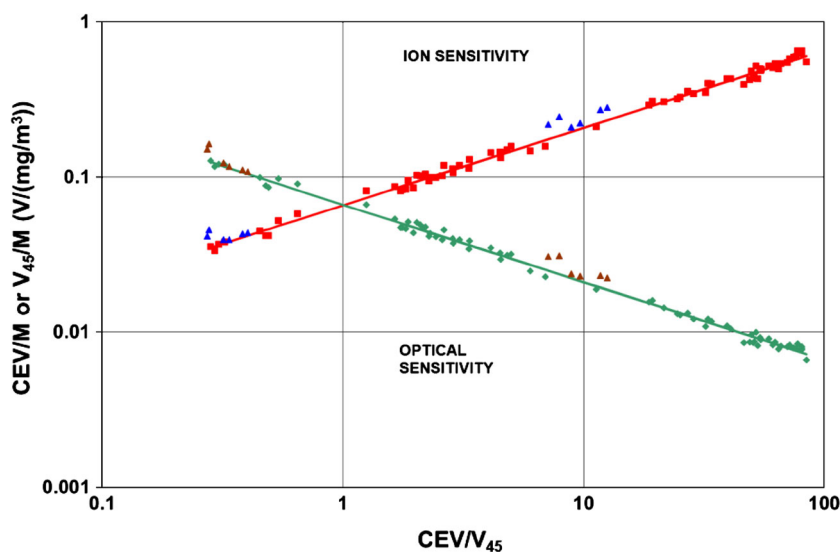


**Figure 1.** **Correlation of ionization-chamber response per unit mass concentration (CEV/M) and angular-scattering response per unit mass concentration ($V_{45}$/M), with the dimensionless ratio of ionization-chamber voltage to angular-scattering voltage measured at 45°, CEV/$V_{45}$.**

backward angles, 15°, 22½°, 30°, 45°, 135°, and 150°, using a precisely machined scattering chamber described in detail in a separate manuscript [11, 12]. The normalized angular scattering data were subsequently used to derive the fractal properties $R_g$ and $D_f$. One port was connected to a DustTrak for mass measurement and another was connected to a $PM_{2.5}$ nozzle where the combustion aerosols were extracted using a pump operating at 1.75 l/min and collected on 2.0-μm, 37-mm Teflon filters for direct mass measurements. Prior to the experiments the pump was calibrated with a Gilian Gilibrator2 calibration system traceable to NIST standards. Each sample was collected for about 10 min–15 min measured from the time the DustTrak reading stabilized in the range of 70 mg/m$^3$–100 mg/m$^3$ (uncorrected) to obtain an accurate mass measurement. The filters were stabilized at ambient temperature at least 24 h before weighing to obtain the mass measurements to evaporate any organic vapors. Each sample was weighed twice and the average reading was used for the calculations. The difference between the two measurements was found to be negligible (typically less than 2 %). A RADWAG 60/220/C/2 analytical balance was used for the mass measurements. At least three filter samples were collected for each combustion source for flaming and smoldering fires during the course of the study. Continuous measurements of the aerosol mass concentrations were made using either a TSI DustTrak 8520 or 8530.

Samples were also flowed to the prototype OPTION sensor that consisted of a well-defined ionization chamber and an optical scattering chamber for discrete measurements of angular scattering at 15° and 30° at a wavelength of 635 nm. The ionization chamber and angular sensitivities were obtained in units of voltage change per unit mass concentration. Angular intensity data from this prototype sensor were also used to derive the radius of gyration for comparison to the values obtained from the six-angle scattering chamber; and the ionization chamber response was used to determine the average number concentration of aggregate particles, average mass of an aggregate, primary particle diameter, and number of primary particles per aggregate as detailed in Eqs. (4)–(12). Similarly, for all of the combustion sources, filter samples were taken for subsequent analysis using Scanning Electron Microscopy (SEM) and Transmission Electron Microscopy (TEM). SEM images were obtained using a JEOL 6400 scanning electron microscope (JEOL, Inc., Tokyo, Japan) from samples collected onto 25-mm polycarbonate membrane filters (Millipore) and coated with gold/palladium before imaging. TEM images were viewed using a JEOL 1220 transmission electron microscope (JEOL, Inc.) from samples directly collected on formvar-coated TEM grids.

## 4. Results and Discussion

### 4.1. Mass Concentrations and Correlations

Aerosol mass concentration is one of the critical measurements in characterizing aerosol properties. Even though the DustTrak is a convenient device for continuous measurement of aerosol mass concentration, accurate calibration of the instrument is important in order for reliable measurements to be obtained. Since this device operates on a light scattering principle, mass concentration measurements

can vary with the type of combustion or the mode of combustion due to differences in particle size, morphology, and chemistry.

Figure 2 above indicates the change of uncorrected DustTrak mass concentration vs time, for smoldering Douglas-fir wood. In this particular experiment, the filter sample was collected from 400 s to 850 s (i.e., for 7 min, 30 s). All the filter measurements in the study were acquired in a similar manner, where smoke was flowed into the smoke box and a sample was drawn out of the box a few minutes after the maximum peak was reached.

In order to calculate the accurate filter mass concentration ($C_m$) the following equation was used.

$$M_{TOT} = C_m \cdot Q_{FLOW} \cdot t$$

where $M_{TOT}$ is the total mass collected on the filter (mg), $Q_{FLOW}$ is the volumetric flow rate (m$^3$/min) and t is the sample collection time (min). Table 1 compares the DustTrak measurements versus the filter sample measurements for aerosols from both flaming and smoldering combustion for the three different combustible samples, with the resultant correction factors being the ratio of DustTrak mass concentration to filter mass concentration.

It was found that the average DustTrak correction factor for the aerosols generated from smoldering combustion was 3.39 (±0.96), and for the aerosols generated from flaming combustion, 3.55 (±0.87). The total average correction factor for aerosols from both flaming and smoldering combustion was 3.47 (±0.90).
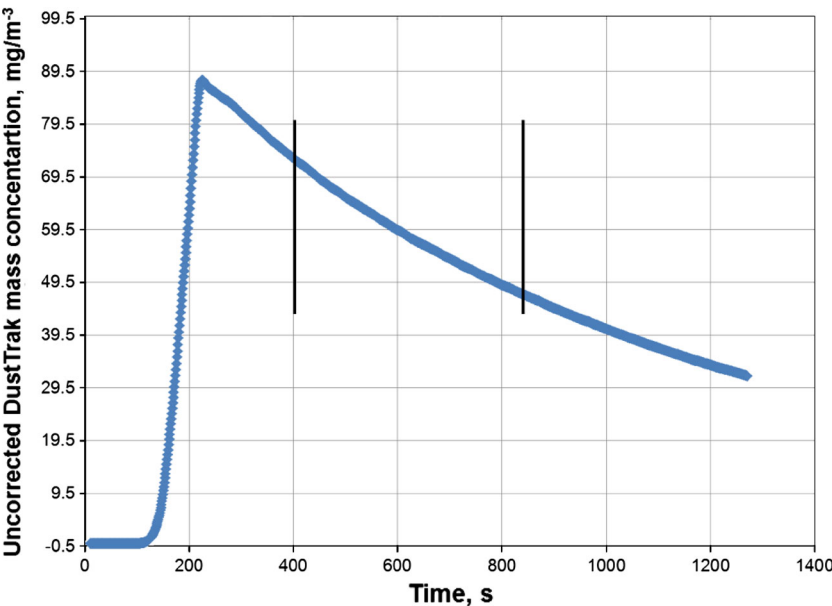


**Figure 2. Variation of the DustTrak mass concentration vs time for smoldering Douglas-fir 3.**

Because the DustTrak uses the light scattering principle to determine the aerosol mass concentration, it is not surprising that the differences in chemistry, size, and morphology from the aerosols generated from flaming and those generated from smoldering combustion sources resulted in two slightly different DustTrak correction factors. However, it is important to note that even though substantial differences may exist between aerosols from flaming combustion compared to those produced from smoldering combustion; the resultant DustTrak correction factors are essentially the same.

Figure 3 summarizes the DustTrak correction factor by different combustion source. Only the DustTrak correction factor for aerosol from smoldering SBR was found to be somewhat smaller (~8 to 9%) than those correction factors obtained for other flaming and smoldering experiments. It is also of interest to note that these values are somewhat higher than those previously reported. Chung et al. [4] reported that when he compared the DustTrak measurements for $PM_{2.5}$ with gravimetric and TEOM measurements, the correction factor was almost 3. In 2002, Yanosky et al. [22] reported a correction factor of 2.57 for $PM_{2.5}$ in indoor air, which was slightly higher than Ramachandran's et al. [18] value of 1.94 obtained for the same type of aerosol. The data in this report were obtained for two DustTrak models 8520 and 8530, and no difference was found between the two for the resultant correction factors.

**Table 1**
**Gravimetric Measurements of the Aerosols of Interest from DustTrak and Filter Measurements**

| | Aerosols from smoldering combustion | | | Aerosols from flaming combustion | | |
|---|---|---|---|---|---|---|
| | DustTrak mass conc. ($mg/m^3$) | Filter mass conc. ($mg/m^3$) | Correction factor | DustTrak mass conc. ($mg/m^3$) | Filter mass conc. ($mg/m^3$) | Correction factor |
| Douglas-fir-1 | 57.97 | 15.91 | 3.64 | 66.59 | 24.76 | 2.69 |
| Douglas-fir-2 | 62.60 | 20.75 | 3.02 | 84.49 | 17.46 | 4.84 |
| Douglas-fir-3 | 49.58 | 15.24 | 3.25 | 48.66 | 19.59 | 2.48 |
| Douglas-fir-4 | 51.76 | 15.71 | 3.29 | 78.90 | 19.05 | 4.14 |
| Douglas-fir-5 | 74.52 | 17.14 | 4.35 | N/A | N/A | N/A |
| Pgh coal-1 | 46.56 | 11.43 | 4.07 | 61.94 | 13.33 | 4.65 |
| Pgh coal-2 | 68.36 | 21.98 | 3.11 | 69.06 | 17.14 | 4.03 |
| Pgh coal-3 | 59.97 | 16.33 | 3.67 | 54.08 | 15.88 | 3.41 |
| Pgh coal-4 | 89.20 | 28.57 | 3.12 | 59.37 | 19.64 | 3.02 |
| Pgh coal-5 | N/A | N/A | N/A | 62.33 | 19.78 | 3.15 |
| Pgh coal-6 | N/A | N/A | N/A | 60.97 | 13.33 | 4.57 |
| Pgh coal-7 | N/A | N/A | N/A | 70.79 | 32.38 | 2.19 |
| SBR rubber-1 | 46.15 | 24.18 | 1.91 | 53.13 | 24.29 | 2.19 |
| SBR rubber-2 | 57.05 | 22.45 | 2.54 | 68.09 | 18.37 | 3.71 |
| SBR rubber-3 | 59.48 | 17.96 | 3.31 | 40.04 | 13.33 | 3.00 |
| SBR rubber-4 | 67.66 | 14.51 | 4.66 | 58.93 | 16.26 | 3.62 |
| SBR rubber-5 | 51.93 | 31.91 | 1.63 | 54.97 | 13.85 | 3.97 |
| SBR rubber-6 | 61.16 | 11.67 | 5.24 | 50.67 | 10.91 | 4.64 |
| Average | | | 3.39 (±0.96) | | | 3.55 (±0.87) |

Table 2 tabulates the correlations between the DustTrak measurements and the mass measurements obtained from the UCB sensor. The UCB mass concentrations were determined using the correlations shown in Figure 1. In Table 2, the DustTrak measurements are compared to both UCB linear mass measurements and UCB logarithmic mass measurements. The linear UCB mass measurement is derived from the approximate Taylor series expansion of the exponential response of the UCB sensor, while the UCB logarithmic mass measurement utilizes the UCB exponential response without any approximation. For the smoldering fires the ratios of DustTrak mass to filter mass and DustTrak mass to the UCB logarithmic mass correlate very well, with only ~5 % standard deviation. The correlation between the ratio of DustTrak mass to UCB linear mass for smoldering aerosols was found to be slightly higher and may be due to the fact that the ionization measurements were beyond the linear range of the Taylor series expansion. Therefore, the logarithmic values may be more realistic for aerosols from smoldering combustion. It was found that there was very little difference between the two UCB measurements for aerosols from flaming combustion even though the ratios are significantly lower than the DustTrak to filter ratio for these aerosols. When comparing the DustTrak and the gravimetric mass measurements with the mass obtained from the UCB sensor, the latter mass was within ±5–10 % of the former mass measurements, indicating its potential capability for use as a low-cost particle analyzer. The lower ratios of DustTrak mass to UCB mass for aerosols from flaming combustion may be a reflection of their different sizes and morphologies, discussed in greater detail below.
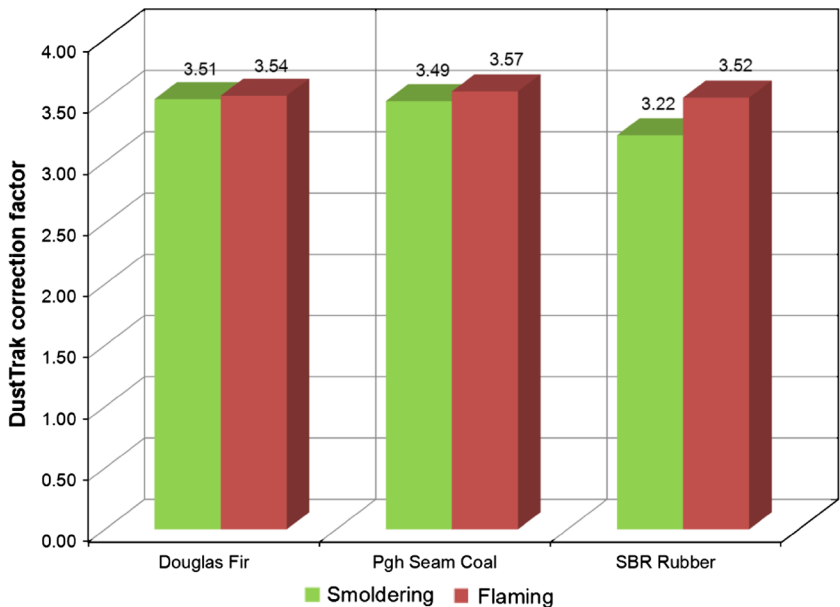


**Figure 3. Average DustTrak correction factors for different smoldering and flaming combustion sources.**

**Table 2**

**Average DustTrak and UCB Sensor Correction Factors for Aerosols Generated from Different Smoldering and Flaming Combustion Sources**

| | Aerosols from smoldering fires | | | | Aerosols from flaming fires | | | |
|---|---|---|---|---|---|---|---|---|
| | DT mass/ filter mass | DT mass/ UCB log mass | DT mass/ UCB linear mass | UCB log mass/ UCB linear mass | DT mass/ filter mass | DT mass/UCB log mass | DT mass/UCB linear mass | UCB log mass/UCB linear mass |
| Douglas-fir-1 | 3.64 | N/A | N/A | N/A | 2.69 | 2.95 | 3.15 | 1.07 |
| Douglas-fir-2 | 3.02 | 3.72 | 4.12 | 1.11 | 4.84 | 2.74 | 3.05 | 1.11 |
| Douglas-fir-3 | 3.25 | 3.15 | 3.54 | 1.13 | 2.48 | N/A | N/A | N/A |
| Douglas-fir-4 | 3.29 | N/A | N/A | N/A | 4.14 | 3.03 | 3.10 | 1.02 |
| Douglas-fir-5 | 4.35 | N/A | N/A | N/A | N/A | N/A | N/A | N/A |
| Pgh seam coal-1 | 4.07 | 2.71 | 2.86 | 1.06 | 4.57 | 2.80 | 3.51 | 1.25 |
| Pgh seam COAL-2 | 3.11 | 3.99 | 4.40 | 1.10 | 4.03 | 2.06 | 2.54 | 1.23 |
| Pgh seam coal-3 | 3.67 | 3.61 | 4.15 | 1.15 | 4.65 | 2.30 | 2.70 | 1.18 |
| Pgh seam coal-4 | 3.12 | N/A | N/A | N/A | 2.19 | 2.26 | 2.64 | 1.17 |
| Pgh seam coal-5 | N/A | N/A | N/A | N/A | 3.41 | N/A | N/A | N/A |
| Pgh seam coal-6 | N/A | N/A | N/A | N/A | 3.02 | 2.07 | 2.51 | 1.21 |
| Pgh seam coal-7 | N/A | N/A | N/A | N/A | 3.15 | 1.93 | 2.34 | 1.21 |
| SBR rubber-1 | 1.91 | 3.58 | 4.02 | 1.12 | 2.19 | N/A | N/A | N/A |
| SBR rubber-2 | 2.54 | 3.28 | 4.00 | 1.22 | 3.71 | 2.18 | 2.37 | 1.09 |
| SBR rubber-3 | 3.31 | N/A | N/A | N/A | 4.64 | 2.03 | 2.27 | 1.11 |
| SBR rubber-4 | 4.66 | N/A | N/A | N/A | 3.00 | N/A | N/A | N/A |
| SBR rubber-5 | 1.63 | N/A | N/A | N/A | 3.62 | N/A | N/A | N/A |
| SBR rubber-6 | 5.24 | N/A | N/A | N/A | 3.97 | N/A | N/A | N/A |
| Average | 3.39 (±0.84) | 3.615 (±0.50) | 4.049 (±0.53) | 1.135 (±0.065) | 3.55 (±0.87) | 2.514 (±0.44) | 2.864 (±0.46) | 1.126 (±0.49) |

## 4.2. Scattering and Extinction Data

Similar to the mass, angular scattering measurements of aerosols vary depending on the source and the mode from which they were generated. Using a six-angle scattering device, angular scattering intensities were obtained to understand the scattering signature of aerosols from the various sources and to quantify differences, where they were found to exist. Figure 4a displays the normalized aerosol angular scattering signatures generated for flaming combustion and Figure 4b displays those for smoldering combustion for the three combustibles tested, namely Douglas-fir wood, Pittsburgh seam coal, and SBR rubber. The data indicate that each of the different aerosols have characteristic angular intensity distributions for both flaming and smoldering modes. It is expected that these distributions reflect differences in the absorbing nature of the individual aerosols (i.e., their chemical composition) as well as differences in the fractal aggregate structure and size.

It is also evident that at forward angles the aerosols generated from smoldering combustion scatter with higher intensities than the aerosols from flaming combustion. In fact, for all the forward angles and two wavelengths measured in these studies, the average scattering intensity for aerosols from smoldering combustion was 36 % higher than the average intensity measured for flaming combustion. In addition to differences in aerosol chemistry, this may be due to the clumping and more compact shape of the aggregates generated from smoldering combustion, which is quite evident in the TEM/SEM images shown later in this report.

Figures 5 and 6 represent the scattering intensities of the fractal aggregates per unit mass concentration obtained at 635 nm wavelength for both flaming and smoldering combustion. The scattering intensity is very similar to $I/I_0$. For aerosols from both flaming and smoldering combustion, the intensities per unit mass concentration are significantly higher (typically, by a factor of 2 to 4) at the lower angles of 15° and 22½°, indicating that the use of forward angles in this range has higher sensitivity for detection and measurement of lower aerosol mass concentrations. In addition, the intensity per unit mass for aerosols from flaming combustion decreases more sharply with increasing angle than does the intensity per unit mass for aerosols from smoldering combustion. Again, these differences are due to the differences in aggregate chemistry and morphology for the flaming and smoldering modes of combustion. Previous theoretical modeling of the angular intensity distributions has shown that very low values of the imaginary component of the index of refraction are necessary in order to reproduce the experimental data for aerosols from smoldering combustion, while much higher values (typical of very high carbon content) are necessary for aerosols from flaming combustion [1].

As discussed in Sects. 2 and 3, light extinction data were obtained using both broadband visible light and monochromatic electromagnetic radiation at $\lambda = 532$ nm while the total scattering coefficient was measured using an integrating nephelometer operating at $\lambda = 520$ nm. From these data and the corresponding mass concentrations, the mass absorption, mass extinction and mass scattering coefficients were calculated and are shown in Table 3. From the data it is quite evident that the mass extinction coefficients for aerosols from flaming combustion are signif-
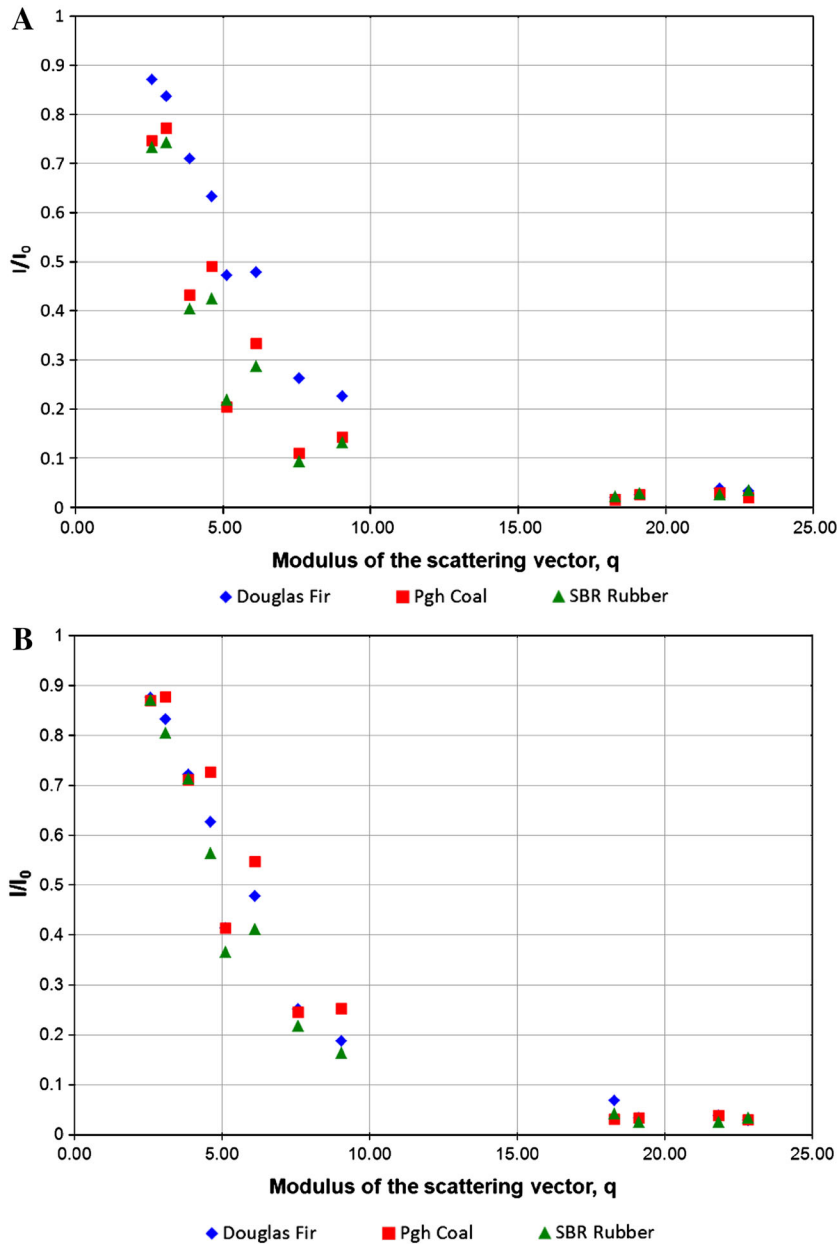
**Figure 4.** **(a) Scattering intensities ($I/I_o$) for aerosols produced from flaming combustion versus modulus of the scattering vector, $q$, for different combustion sources. (b) Scattering intensities ($I/I_o$) for aerosols produced from smoldering combustion versus modulus of the scattering vector, $q$, for different combustion sources.**
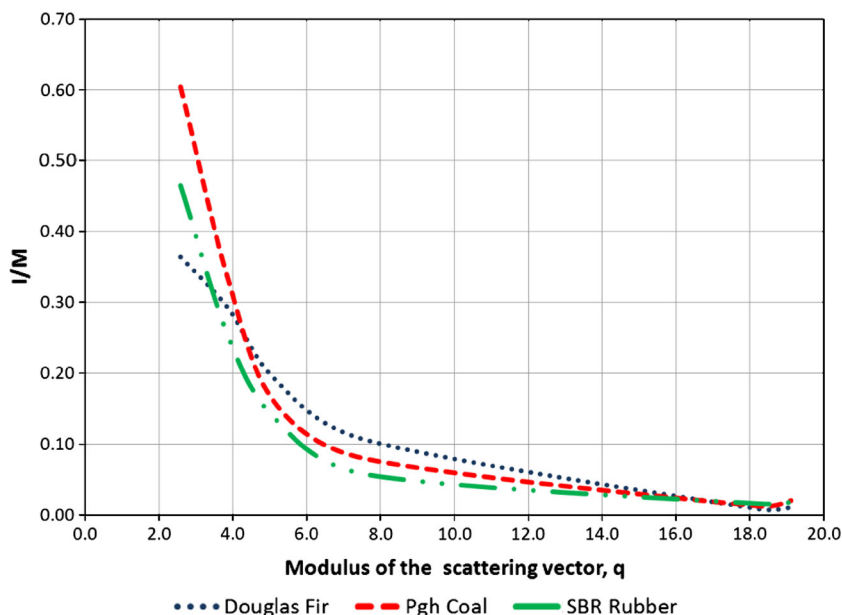
**Figure 5. Scattering intensities per unit mass (I/M) for aerosols from flaming combustion at 635 nm versus the modulus of the scattering vector, q.**

icantly higher than values reported in the literature, while the mass scattering coefficients are relatively lower and constant, resulting in very high mass absorption coefficients (average of 11.3 $m^2$/g compared to an average of 7.5 $m^2$/g reported by Bond and Bergstrom) [1]. The mass extinction coefficients for aerosols from smoldering combustion are in much better agreement with the values that are reported in the literature [1]. Overall, the mass extinction coefficient for aerosols generated from flaming combustion was more than twice that for aerosols from smoldering combustion. It is also worth noting that the mass extinction coefficients for aerosols from smoldering combustion are almost entirely due to scattering (average albedo is 0.87) while those from aerosols from flaming combustion are dominated by absorption (average albedo is 0.27).

## 4.3. Fractal Aggregate Properties

As stated in Sect. 3, the response of the prototype ion chamber was obtained to quantify fractal aggregate properties and to compare these to the values obtained from the UCB sensor measurements. These data, along with parameters from the optical scattering data, were used to calculate properties of the fractal aggregates. The results of the angular scattering computations provided the radius of gyration ($R_g$) and fractal dimension ($D_f$). From the ion chamber data, the number mean diameter ($d_g$), number of aggregates per cubic centimeter ($N$), mass of a fractal aggregate ($M_a$), diameter of primary particle ($d_p$), and number of primary particles
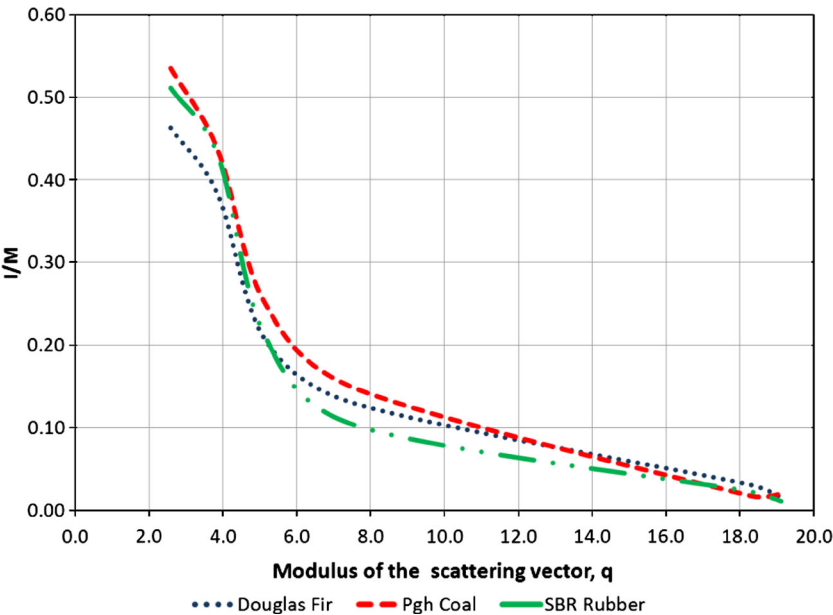
**Figure 6. Scattering intensities per unit mass (I/M) for aerosols from smoldering combustion at 635 nm versus the modulus of the scattering vector, q.**

**Table 3**
**Scattering, Extinction and Absorption Coefficients for Aerosols for the Different Combustion Sources**

| | $\sigma_{ext}$ (532 nm) | $\sigma_{sca}$ (532 nm) | $\sigma_{abs}$ (532 nm) | $\sigma_{ext}$ (visible) | Albedo |
|---|---|---|---|---|---|
| _Flaming_ | | | | | |
| Douglas-fir | 16.704 | 2.490 | 14.214 | 13.700 | 0.149 |
| Pgh coal | 13.603 | 4.368 | 9.197 | 11.877 | 0.321 |
| SBR rubber | 16.062 | 5.447 | 10.615 | 11.102 | 0.339 |
| Average of all tests | 15.456 | 4.102 | 11.342 | 12.226 | 0.270 |
| _Non flaming_ | | | | | |
| Douglas-fir | 7.594 | 6.607 | 0.987 | 4.279 | 0.870 |
| Pgh coal | 7.036 | 6.213 | 0.823 | 5.218 | 0.883 |
| SBR rubber | 8.272 | 7.166 | 1.107 | 4.513 | 0.866 |
| Average of all tests | 7.634 | 6.662 | 0.972 | 4.670 | 0.873 |

per aggregate ($n_p$) were also calculated using Eqs. (4)–(12). These ion chamber calculations were compared with similar calculations obtained from the UCB sensor data and are tabulated in Table 4. These data provide a unique and complete description of the physical properties of the differing fractal aggregates generated from flaming and smoldering fires. It should be noted that when calculating the fractal properties using the UCB device, the _Rg_ was calculated using average

**Table 4**
**Aerosol Particle Properties Calculated from the UCB Sensor and OPTION Sensor**

|  | Pgh coal | | Douglas-fir | | SBR rubber | |
|---|---|---|---|---|---|---|
|  | UCB data | Ion chamber | UCB data | Ion chamber | UCB data | Ion chamber |
| *Flaming* | | | | | | |
| $R_g$ | 430 | 325 | 454 | 270 | 410 | 252 |
| $d_g$ | 241 | 223 | 254 | 290 | 230 | 230 |
| N | 865277 | 1871019 | 1121610 | 1678818 | 1083182 | 2560975 |
| $M_a$ | 2.61E$-$14 | 8.75E$-$15 | 3.25E$-$14 | 1.57E$-$14 | 2.25E$-$14 | 8.94E$-$15 |
| $d_p$ | 33 | 23 | 35 | 41 | 33 | 36 |
| $n_p$ | 755 | 1535 | 755 | 4517 | 754 | 729 |
| Mass conc. | 23 | 16 | 20 | 19 | 24 | 19 |
| $D_f$ | 1.85 | 1.77 | 1.85 | 2.3 | 1.85 | 1.73 |
| *Smoldering* | | | | | | |
| $R_g$ | 204 | 227 | 193 | 237 | 181 | 237 |
| $d_g$ | 249 | 400 | 235 | 349 | 221 | 383 |
| N | 589123 | 648010 | 685364 | 780524 | 921840 | 608331 |
| $M_a$ | 2.97E$-$14 | 3.45E$-$14 | 2.43E$-$14 | 2.91E$-$14 | 2.02E$-$14 | 4.04E$-$14 |
| $d_p$ | 102 | 82 | 97 | 60 | 91 | 81 |
| $n_p$ | 28 | 144 | 28 | 343 | 28 | 424 |
| Mass conc. | 16 | 19 | 16 | 22 | 18 | 23 |
| $D_f$ | 2.21 | 2.30 | 2.21 | 2.22 | 2.21 | 2.17 |

*Rg/dg* ratios obtained from a previous study [17]. Also, constant values were used for $D_f$, where for aerosols generated from flaming fires, $D_f = 1.85$ was used, while for aerosols generated from smoldering fires, $D_f = 2.1$ was used. The detailed theory and calculations for both the ion and optical responses of the UCB sensor are published elsewhere [13].

Analysis of Table 4 data shows several distinctive trends relative to the aerosols from flaming versus those from smoldering combustion. First, aerosols from flaming combustion have higher values of $R_g$, but smaller values of primary particle diameter, $d_p$. The fractal dimension, $D_f$, of aerosols from flaming combustion have an average value of 1.80, while for aerosols from smoldering the average is 2.26, with both values consistent with data from the literature. Flaming combustion produces fractal aggregates with small primary particles but large numbers of primary particles per aggregate, with the result that the average mass of a fractal aggregate is more than three times lower than the corresponding average mass of FAs from smoldering combustion. It is also interesting to note that the average number mean diameter calculated for FAs from flaming combustion is 30 % less than the average for smoldering combustion, while the average $R_g$ for FAs from flaming combustion is 30 % higher. When comparing these data with the measurements obtained from the UCB sensor, the values are in good agreement. One interesting phenomenon is that the calculated $R_g$ with the UCB sensor is higher than the ion chamber measurements for aerosols generated from flaming
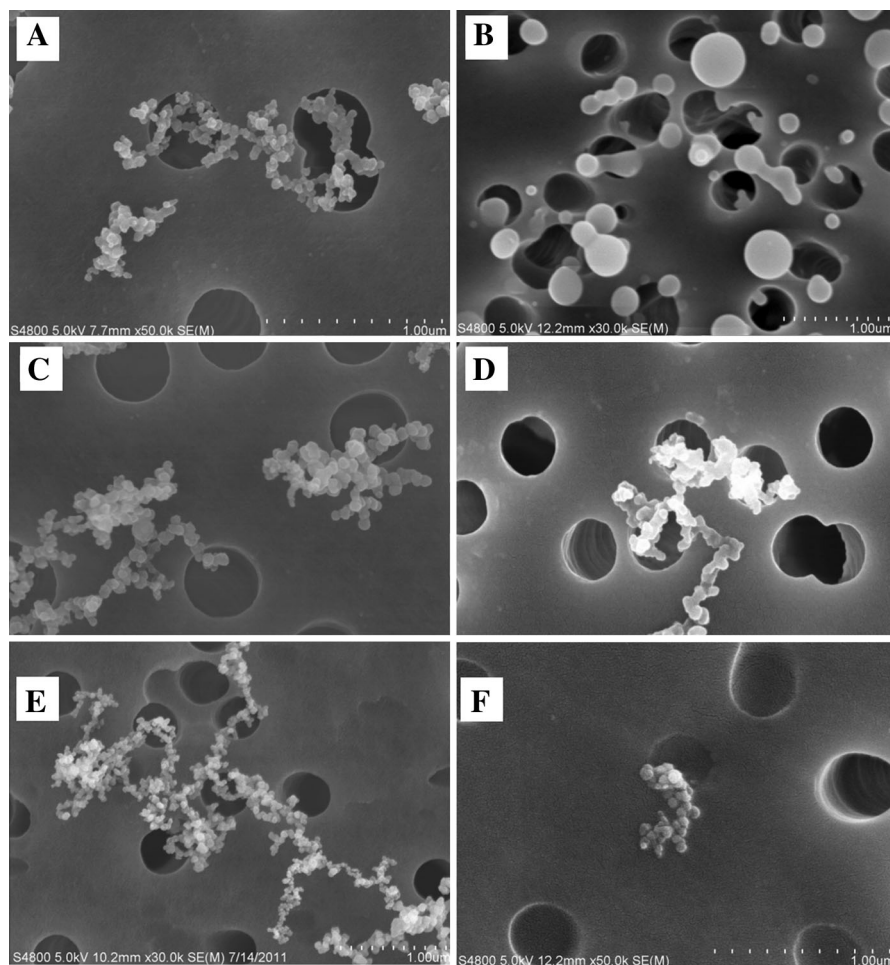
**Figure 7.   SEM images of (a) flaming and (b) smoldering coal, (c) flaming and (d) smoldering SBR rubber & (e) flaming and (f) smoldering Douglas-fir wood. Note that the large pores are from the filter paper background.**

combustion, but the reverse is true for aerosols generated from smoldering combustion, where the UCB measurement is smaller than the ion chamber measurements.

Representative SEM/TEM photographs from samples collected from flaming and smoldering combustion for combustible materials used in the present study are shown in Figures 7 and 8. It is evident from these photographs that the aerosols produced from flaming combustion are fractal aggregates with relatively small primary particles and elongated, chain-like morphologies (smaller $D_f$), while those produced from smoldering combustion have larger primary particles and clumped
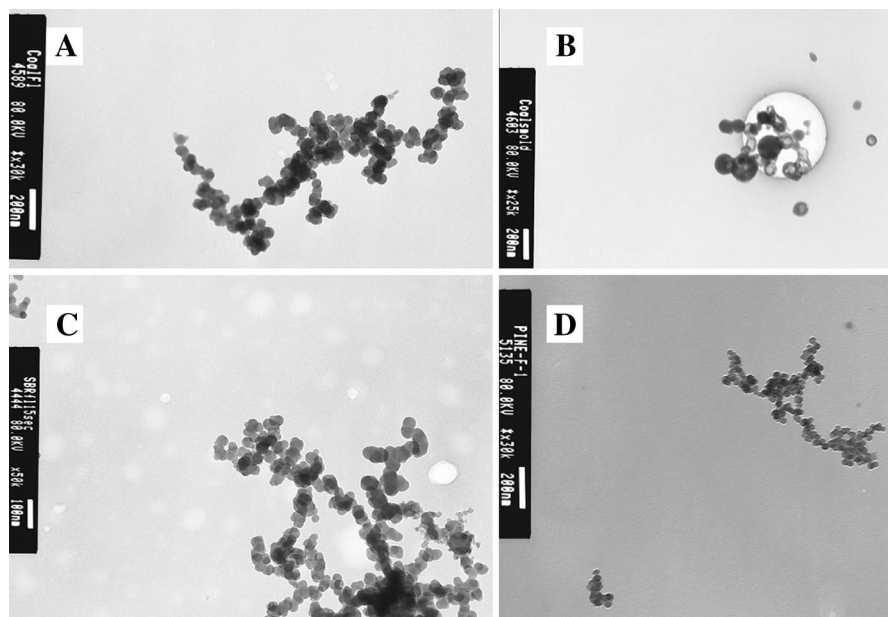
**Figure 8.** SEM images of (a) flaming and (b) smoldering coal, (c) flaming SBR rubber, and (d) flaming Douglas-fir wood.

or more densely packed morphologies (larger $D_f$). These images are consistent with the aggregate properties presented in Table 4 and agree qualitatively with results from previous studies. In these previous studies, soot particles produced from fuel-lean and stoichiometric combustion generally produced a more elongated, chain-like structure with very little overlap of individually connected particles. As the combustion became more fuel-rich, the aggregate structure gradually evolved to the more compact form, with fractal dimensions increasing with the fuel–air ratio [13]. When comparing the microscopic measurements with the values calculated from the experimental data, there is reasonably good agreement. For instance, the $R_g$ (∼400 nm) and $d_p$ (∼50 nm) measurements obtained for aerosols from the flaming SBR images are in close agreement with the calculated values of 280 nm and 35 nm, respectively, from Table 4. The images are being further analyzed in much detail using commercial software and the results are to be published in a future separate manuscript.

## 4.4. Sensor Response Data

The data for the prototype OPTION sensor are also analyzed in terms of its responses per unit mass concentration as functions of the dimensionless ratios of ionization signal voltage, *CEV*, to optical scattering voltages at both 15° and 30°, $V_{15}$ and $V_{30}$, respectively. As previously mentioned in the Introduction, these sensitivities are found to vary with the signal ratios—a dimensionless and easily measured quantity. The results indicate that it is possible to utilize this simple ratio to
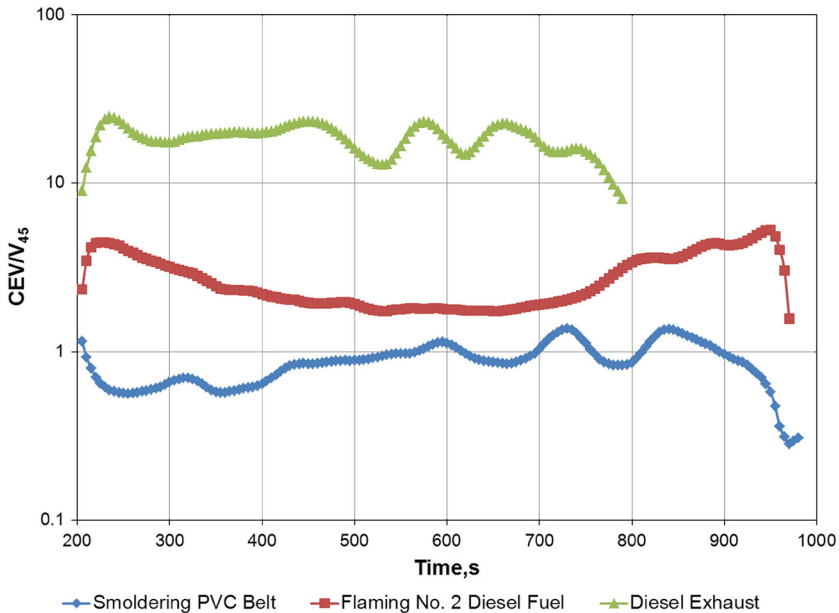
**Figure 9.   Ratio of ionization response to photoelectric response for aerosols from smoldering PVC, a diesel fuel pool fire, and diesel exhaust.**

define regions of sensitivity and regions of discrimination that can aid in the fire detection process as well as discriminate against other non-fire related sources. Application of the sensor as a smoke detector, for instance, in areas that may contain significant levels of diesel exhaust particles, has been previously shown to work quite well, where DPM has a very high value of both $CEV/V_{15}$ and $CEV/V_{30}$, allowing for very good discrimination capabilities [11].

In order to understand this phenomenon better, a series of experiments were conducted using polyvinyl chloride (PVC) belt, a common fire-retardant conveyer belt used in the mining industry, and No. 2 diesel fuel, and the responses of the ion chamber and optical chamber were measured. In Figure 9, these data are compared to the data obtained for aerosols produced from the exhaust of a diesel engine, where it is evident that the ratio of ionization response to optical response varies with flaming and smoldering combustion as well as with diesel exhaust. For smoldering combustion, consistent with results from the previous study, the average measured ratio was 1 or less than 1; for flaming combustion, this response ratio was in the range of 1 to 8; for the diesel exhaust, this response ratio was at least 10 or greater. Large differences such as these in this simple response ratio have significant potential not only to discriminate between aerosols from fires and those from diesel exhausts, but also to discriminate between flaming and smoldering modes of combustion. This latter capability could further be used to qualitatively assess the relative levels of carbon in the fractal aggregates.

# 5. Conclusion

Overall, when the mass concentration measurements of aerosols generated from different combustion sources using TSI DustTrak Models 8520 and 8530 are compared with gravimetric filter samples, a constant ratio of ~3.5 is obtained which can be used in future studies involving combustion-generated aerosols. Because the DustTrak uses light scattering to measure the mass concentration, the factory calibration using Arizona road dust does not appear suitable for the type of combustion aerosols generated from fires involving coal, wood, and rubber, and most probably other combustion sources, because of their smaller particle size ($\leq$0.5 µm). It was found from the data acquired during this study that the DustTrak correction factor for aerosols generated from smoldering combustion is 3.39, compared to a value of 3.55 for the aerosols generated from flaming combustion, with an overall average value of 3.47. These values are significantly higher than previously reported values that ranged from 1.94 to 3.0, and should be applied in any application where the DustTrak devices may be used to measure combustion-generated aerosols. In addition, to the knowledge of the authors, this is the first report to distinguish two DustTrak correction factors for aerosols generated from both flaming and smoldering combustion.

When comparing the DustTrak mass concentration measurements with the mass concentrations calculated from the UCB sensor data, the numbers correlate very well, indicating the potential capability to use the modified UCB sensor as a low-cost particle monitor. The measurements obtained from TEM/SEM images are also in good agreement with the calculated measurements and tend to further validate the capability of the modified UCB sensor, along with this optical/ionization technique, for measurement and characterization of aerosols produced from combustion.

The data obtained from the ionization chamber response of the OPTION sensor and the UCB sensor above give a comprehensive summary of the optical and physical properties of fractal aggregates generated from a variety of combustible sources for both flaming and smoldering combustion. The data conclusively indicate that while all of the aerosols generated could be described as fractal aggregates, significant differences in their morphology and size exist both as a function of combustion source and combustion mode, and that these differences result in different fractal properties which can subsequently be used to describe the fractal aggregates in analytical terms. In addition, this fundamental information on the optical and physical properties of smoke particles generated from combustion processes can be used toward the design and modification of more reliable and effective smoke detectors which will be beneficial for the safety and health of miners.

# Acknowledgments

# References

1. Bond TC, Bergstrom RW (2006) Light absorption by carbonaceous particles: an investigative review. Aerosol Sci Technol 40:27–67
2. Butler KM, Mulholland GW (2004) Generation and transport of smoke components. Fire Technol 40:149–176
3. Blomqvist P, Bror P, Simonson M (2007) Fire emissions of organics into the atmosphere. Fire Technol 43:213–231
4. Chung A, Chang DPY, Kleeman MJ, Perry KD, Cahill TA, Dutcher D, McDougall EM, Stroud K (2001) Comparison of real-time instruments used to monitor airborne particulate matter. J Air Waste Manag Assoc 51:109–120
5. Edwards JC, Morrow GS (1995) Development of coal combustion sensitivity tests for smoke detectors. United States Department of Interior, Report of Investigation 9551: 1–12
6. Farias TL, Carvalho MG, Koylu UO, Faeth GM (1995) Computational evaluation of approximate Rayleigh–Debye–Gans/fractal-aggregate theory for the absorption and scattering properties of soot. J Heat Transf 117:152–159
7. Kelly WP, Mcmurry PH (1992) Measurement of particle density by inertial classification of differential mobility analyzer generated monodisperse aerosols. Aerosol Sci Technol 17:199–212
8. Kingham S, Durand M, Aberkane T, Harrison J, Wilson JG, Epton M (2006) Winter comparison of TEOM, MiniVol and DustTrak PM10 monitors in a woodsmoke environment. Atmos Environ 40:338–347
9. Kinsey JS, Mitchell WA, Squier WC, Linna K, King FG, Logan R, Dong YJ, Thompson GJ, Clark NN (2006) Evaluation of methods for the determination of diesel-generated fine particulate matter: physical characterization results. J Aerosol Sci 37:63–87
10. Lehocky AH, Williams PL (1996) Comparison of respirable samplers to direct-reading real time aerosol monitors for measuring coal dust. Am Ind Hyg Assoc J 57:1013–1018
11. Litton CD (2002) The use of light scattering and ion chamber responses for the detection of fires in diesel contaminated atmospheres. Fire Saf J 37:409–425
12. Litton CD (2009) Laboratory evaluation of smoke detectors for use in underground mines. Fire Saf J 44:387–393
13. Litton CD, Smith KR, Edwards R, Allen T (2004) Combined optical and ionization measurement techniques for inexpensive characterization of micrometer and submicrometer aerosols. Aerosol Sci Technol 38:1054–1062
14. Litton CD (1977) A mathematical model for ionization-type smoke detectors and the reduced source approximation. Fire Technol 13:28–261
15. Litton CD (1979) Optimizing ionization-type smoke detectors. Fire Technol 15:25–42
16. Moosmuller H, Arnott WP, Rogers CF, Bowen JL, Gillies JA, Pierson WR, Collins JF, Durbin TD, Norbeck JM (2001) Time-resolved characterization of diesel particulate emissions. 2. Instruments for elemental and organic carbon measurements. Environ Sci Technol 35:1935–1942
17. Perera IE, Litton CD (2011) A detailed study of the properties of smoke particles produced from both flaming and non-flaming combustion of common mine combustibles. Fire Saf Sci 10:213–226. doi:10.3801/IAFSS.FSS.10-213
18. Ramachandran G, Adgate JL, Hill N, Sexton K, Pratt GC, Bock D (2000) Comparison of short-term variations (15-minute averages) in outdoor and indoor PM2.5 concentrations. J Air Waste Manag Assoc 50:1157–1166
19. Slowik JG et al (2007) An inter-comparison of instruments measuring black carbon content of soot particles. Aerosol Sci Technol 41:295–314

20. Sorensen CM (2001) Light scattering by fractal aggregates: a review. Aerosol Sci Technol 35:648–687
21. Wolin SD, Noah LR, Frederic L, James AM, Frederick WM, Jose LT (2001) Measurements of smoke characteristics in HVAC ducts. Fire Technol 37:363–395
22. Yanosky JD, Williams PL, MacIntosh DL (2002) A comparison of two direct-reading aerosol monitors with the federal reference method for PM2.5 in indoor air. Atmos Environ 36:107–113